Central European Journal of Energetic Materials
ISSN 1733-7178; e-ISSN 2353-1843

Cent. Eur. J. Energ. Mater. 2024, *21*(4): 429-449; DOI 10.22211/cejem/198409
Article is available in PDF-format, in colour, at:
https://ipo.lukasiewicz.gov.pl/wydawnictwa/cejem-woluminy/vol-21-nr-4/

Research paper

Preparation of Graphene-based Cu-MOF Derivative Catalysts and Their Catalytic Performance for Cyclotrimethylenetrinitramine Thermal Decomposition

Jiao Zhang[1)], **Taixin Liang***[,2)]

[1)] *Internal Medicine Department of the North Hospital of Taiyuan Taihang Hospital, Taiyuan 030000, China*

[2)] *School of Environment and Safety Engineering, North University of China, Taiyuan 030051, China*

* *E-mail:* liangtx2006@126.com

Abstract: In order to improve the thermal decomposition performance of cyclotrimethylenetrinitramine (RDX), graphene-based Cu-MOF derivative catalysts were prepared by solvothermal and heat treatment. Transition metal ions were ligated to the surface of graphene oxide (GO) by organic ligands, and then heat-treated to obtain two-dimensional reduction-oxidation graphene-based metal cluster catalysts. The morphology and structure of these catalysts at different temperatures and their effects on the thermal decomposition of RDX were studied. The results showed that the prepared GO/Cu-MOF has a small particle size and good dispersibility. At 300 °C, the catalyst exhibited a porous structure. Thermal analysis showed that the decomposition temperature of RDX was reduced by the addition of a small amount of this catalyst, which may be due to the good conductivity of graphene oxide and the strong gain and loss electron ability of the metal clusters. The presence of graphene oxide increases the catalytic activity of metal clusters, and the metal clusters and graphene oxide have a positive synergistic effect, thus improving the thermal decomposition performance of RDX.

Keywords: cyclotrimethylenetrinitramine, Cu-MOF, graphene oxide, thermal decomposition performance

1 Introduction

Ammonium nitrate explosive, as a kind of high-energy density energetic material, has been widely used in military, national defense and other fields because of its strong power, high detonation velocity and stable performance [1, 2]. As a third generation simple military high explosive, cyclotrimethylenetrinitramine (RDX) has a detonation velocity of 8640 m/s at a density of 1.767 g/cm^3, with great power, second only to octogen (HMX). RDX is a typical high energy density nitramine explosive, and is also the main high-energy ingredient and oxidant in solid propellants [3-5]. RDX's central structure is a rigid six-membered ring composed of alternate C and N atoms, as shown in Figure 1. It has a high activation energy and a stable molecular structure, so it is not easily decomposed at high temperature, and has good stability. All of these factors lead to a high melting point for RDX, which greatly limits the application and promotion of RDX in solid propellants and gun propellants. Therefore, improving the thermal decomposition performance of RDX is of great significance [6, 7].

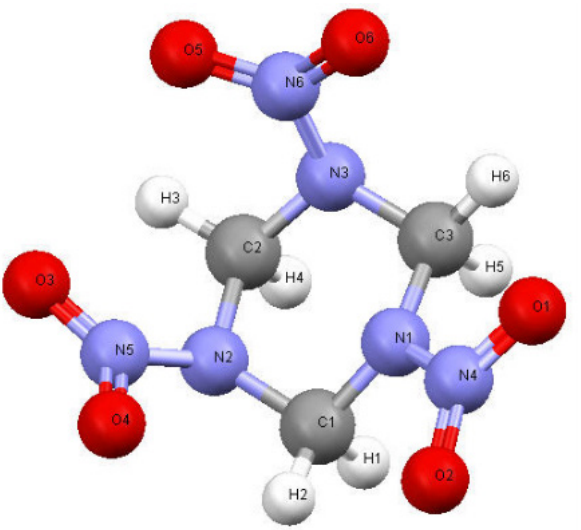

Figure 1. The molecular structure of RDX [8]

Nanocatalysts have small particle size, large specific surface area, many surface atoms and internal lattice defects, so they exhibit excellent catalytic performance and have incomparable advantages over traditional catalysts [9]. The particle size is an important factor affecting the performance of the catalyst. Nanometer aluminium (Al) powder, as a highly efficient accelerant, can not only

improve the explosive power of a nitramine explosive, but also have a good catalytic effect on the decomposition of a nitramine explosive. Zhu *et al.* [10] studied the effect of different Al particle sizes on the thermal decomposition of RDX. The smaller the Al particle size, the stronger the catalytic performance [10]. Incorporation of Al nanoparticles (AlNPs) into RDX catalyzes its thermal decomposition and reduces the pressure index (*n*) of a solid propellant. Xiong *et al.* [11] used ReaxFF molecular dynamics (REAXFF-MD) simulation combined with DFT calculations to study the reaction process of AlNPs catalyzed thermal decomposition of RDX under different initial pressures, and revealed the influence mechanism of AlNPs on the sensitivity of RDX thermal decomposition to pressure from different perspectives. In addition, nano-Cu powder, nano-Ni powder and nano-Mg powder all have catalytic effects on the decomposition of RDX [12-14].These nano-metal powders significantly improve the energy density, thermal decomposition ability, burning rate and detonation performance of nitramine explosives. However, these nanomaterials are very unstable, and the active atoms on the surface are prone to agglomerate to form nanoclusters at high temperatures. Even if the agglomerates have been broken, they will agglomerate again, ultimately reducing the effective surface area and thus affecting their catalytic performance [15-17]. Among various factors, the dispersion technology of nanomaterials is the key to their application in the field of nitramine explosives. Strategies to increase the active site, either by reducing the size of the catalyst clusters, or by improve the dispersion of low-scale particles that increase the external exposure surface, have been shown to be effective. Graphene oxide (GO) is a new type of two-dimensional carbon material, which contains a variety of oxygen-containing functional groups on the surface, has good thermal conductivity, excellent flexibility and ductility, and has a very large specific surface area on the horizontal plane [18]. In composites containing GO, GO acts as a dispersant to make the nanomaterials disperse well on their surfaces, thereby increasing the catalytically effective active sites, which can accelerate the charge transport of the nanocomposites and improve their catalytic performance. At the same time, GO has a synergistic effect with nanoparticles, which can further enhance the catalytic decomposition performance [19].

Yin *et al.* used $CuFe_2O_4$/g-C_3N_4 nanocomposites, commonly used in photocatalysis, as combustion catalysts. $CuFe_2O_4$/g-C_3N_4 nanocomposites were designed and prepared by an *in situ* solvothermal method. The synergistic effects of $CuFe_2O_4$ nanoparticles and graphite-phase carbon nitride (g-C_3N_4) on the thermal decomposition of RDX and ammonium perchlorate (AP) were systematically analyzed. $CuFe_2O_4$/g-C_3N_4 nanocomposites transfer the decomposition of RDX to lower temperatures with increased g-C_3N_4 content, while AP shows the opposite

trend. In addition, the thermal decomposition stage and related products of AP and RDX were detected by thermogravimetric mass spectrometry (TG-MS), which showed that the $CuFe_2O_4$/g-C_3N_4 catalyst reduced the decomposition temperature and changed the decomposition process, and had a better catalytic decomposition effect on both AP and RDX [20]. Wan *et al.* [20] successfully prepared $MgFe_2O_4$-GO nanocomposites by the *in-situ* growth method, and characterized them by XRD, FTIR, Raman spectroscopy, SEM and TEM. The results demonstrated that $MgFe_2O_4$-GO nanocomposites can significantly reduce the decomposition temperature and apparent activation energy of AP from 406.8 to 306.5 °C and 161.0 kJ/mol, respectively, and increase the decomposition heat of AP from 654.7 to 1183.2 J/g. The thermal decomposition temperature of RDX is also reduced from 242.3 to 234.6 °C. $MgFe_2O_4$-GO nanocomposites prepared by the *in-situ* growth method exhibited better catalytic decomposition performance than pure $MgFe_2O_4$, a physical mixture $MgFe_2O_4$-GO and self-assembled $MgFe_2O_4$-GO [21]. Using the multiple self-assembly method, Liu *et al.* [16] prepared $CuFe_2O_4$/GO nanoparticles. Compared with the catalytic performance of GO alone, the catalytic activity of the $CuFe_2O_4$ composite on RDX is much higher [16].

In recent years, Metal organic framework (MOF) materials have been gradually applied in the catalytic research of energetic materials. A MOF structure is a kind of organic-inorganic hybrid, an ultra-low density porous material, which binds metal ions to organic ligands through coordination covalent bonds [22]. MOFs have the advantages of high porosity, large surface size and adjustable structure. There are many kinds of MOF materials formed according to different metal and organic ligands, among which Cu-MOF is the most popular, widely used in chemical reduction, biological adsorption [23], catalytic oxidation [24], hydrogen evolution reactions and electrocatalysis [25]. In the present work, we prepared graphene-supported metal Cu nanoparticle catalysts by calcination of organic ligands at high temperature through the action of metal-organic skeleton nodes and covalent coordination bonds, accurately anchored the site and regulated the activity of the metal ion catalyst, and studied the influence of catalysts with different structures on the thermal decomposition ability of RDX.

2 Experimental

2.1 Experimental reagents

The experimental reagents were copper sulfate pentahydrate (99.9%), 2-aminoterephthalic acid (98%), *N*,*N*-dimethylformamide (99.9%), acetonitrile (99.9%), graphene oxide (99.9%) produced by Aladdin Chemical Reagent Co., Ltd.,

anhydrous ethanol (99.7%) produced by Sinopath Chemical Reagent Co., Ltd. and RDX (95%) produced by the Institute of Modern Chemistry in Xi ‘an. All reagents were commercially purchased and analytically pure, and need not be further purified before use.

2.2 Experimental instruments

The experimental instruments used were a FA1004N electronic analytical balance produced by Shanghai Jinghai Instrument Co., Ltd., a KQ2200B ultrasonic cleaner produced by Kunshan Ultrasonic Instrument Co., Ltd., a DZF-6020 electric thermostatic blast drying oven produced by Shanghai Jinfu Experimental Instrument and Equipment Co., Ltd., an ALPHA produced by Christ Company in Germany 2-4 LD freeze-dryer, a TG16-WS high speed centrifuge produced by Shanghai Anting Scientific Instrument Factory, a STA-449C thermogravimetric analyzer and a DSC-404 F3 differential scanning calorimeter produced by German Nez Instrument Manufacturing Co., Ltd.

2.3 Preparation of Cu-MOF, GO/Cu-MOF, GO/Cu-MoF-300, GO/Cu-MOF-400 composite materials

Cu-MOF was prepared by a one step solvothermal method. The specific synthesis route was as follows: $CuSO_4 \cdot 5H_2O$ (2.8 mmol) and 2-aminoterephthalic acid (1.2 mmol) were added to a mixture of DMF/acetonitrile (80 mL, volume ratio 1:1), and magnetically stirred for 5 min. The mixture was then transferred to a 100 mL Teflon lined stainless steel autoclave and reacted at 110 °C for 3 h. The suspension obtained was washed alternately with DMF and ethanol, centrifuged, and freeze-dried to obtain a dark green solid powder, Cu-MOF. The preparation of GO/Cu-MOF composites was similar to that of Cu-MOF. GO (20 mg) was treated with ultrasound in the mixed solution for a sufficient time, while stirring to form a uniform suspension. The remaining steps remain the same.

By TGA, the prepared GO/Cu-MOF composites were calcined at 300 and 400 °C, respectively, and calcined at these two temperatures for 2 h, to obtain different types of two-dimensional catalysts, which were ground into a powder, named GO/Cu-MoF-300 and GO/Cu-MoF-400.

2.4 Preparation of RDX/GO/Cu-MOF, RDX/GO/Cu-MOF-300 and RDX/GO/ Cu-MOF-400

The composite material (3 mg) and RDX (97 mg) were accurately weighed on an electronic balance and fully ground to obtain RDX/GO/Cu-MOF, RDX/GO/Cu-MOF-300 and RDX/GO/Cu-MOF-400, respectively. The composite material accounted for 3% of the mass.

3 Results and Discussion

3.1 Characterization of Cu-MOF, GO/Cu-MOF, GO/Cu-MOF-300, GO/Cu-MOF-400

The morphologies of the different samples were observed through scanning electron microscopy, as shown in Figure 2. Figure 2(a) shows the original RDX particles used, which appear as elliptical-spheroidal particles with an average particle size between 2-5 μm. Figure 2(b) shows that GO has a lamellar structure with rough surface folds and obvious agglomeration, which may be the result of the interaction between oxygen-containing functional groups and interlayer van der Waals forces. The prepared pure Cu-MOF (Figure 2(c)) had a spherical structure with many small particles attached to the surface. After the addition of GO, the agglomeration of Cu-MOF was hindered and the number of particles increased significantly. At the same time, the formation of Cu-MOF also inhibited the re-accumulation of GO, indicating that GO/Cu-MOF composites were successfully prepared (Figure 2(d)). GO/Cu-MOF-300 (Figure 2(e)) and GO/Cu-MOF-400 (Figure 2(f)) were obtained after calcination of GO/Cu-MOF at 300 and 400 °C for 2 h, respectively. At 300 °C, the spherical structure disappeared and many pores appeared, and the characteristic channel of the MOF appeared, indicating that the MOF structure had partially collapsed. After treatment at 400 °C, the particles became smaller and the generated pores had disappeared, indicating that the MOF structure was completely decomposed.

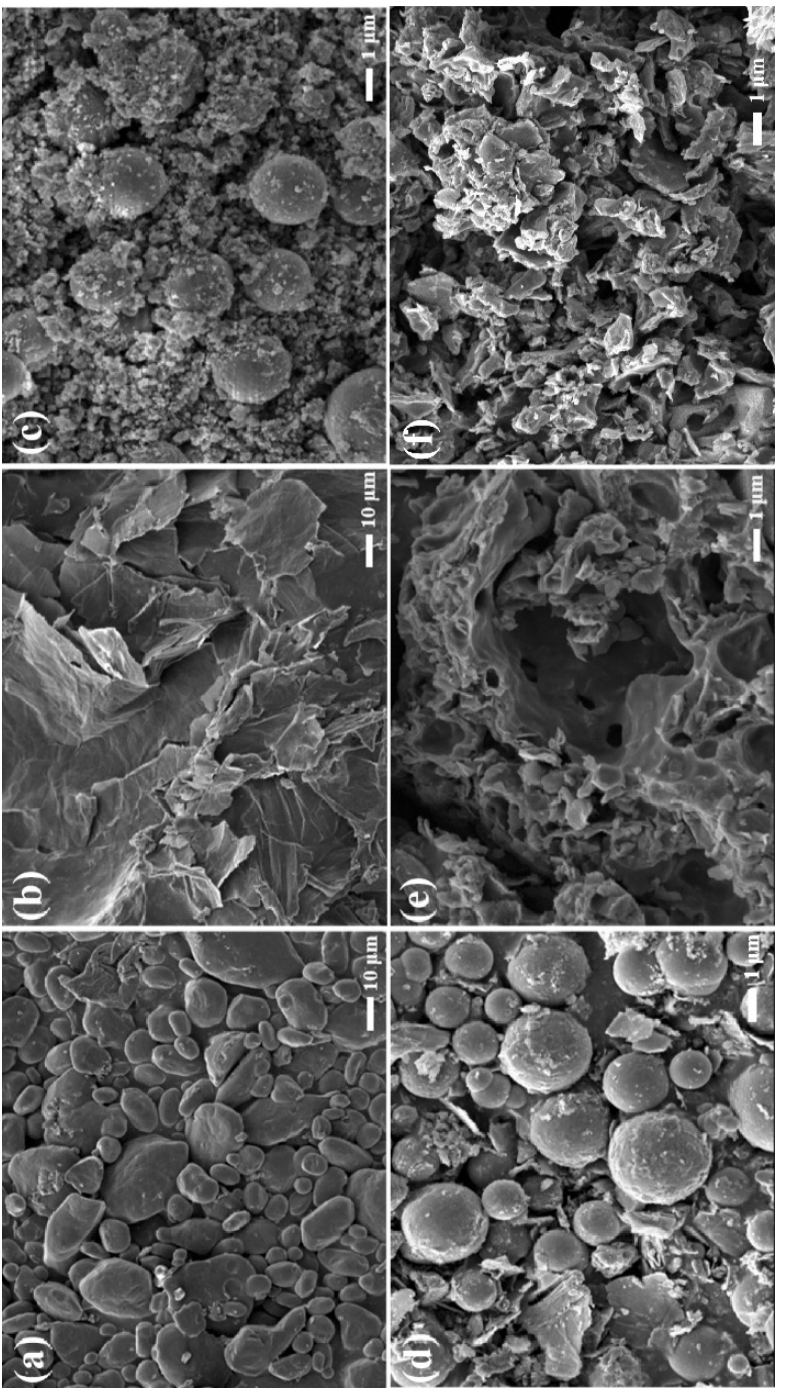

Figure 2. SEM images of RDX (a), GO (b), Cu-MOF (c), GO/Cu-MOF (d), GO/Cu-MOF-300 (e) and GO/Cu-MOF-400 (f)

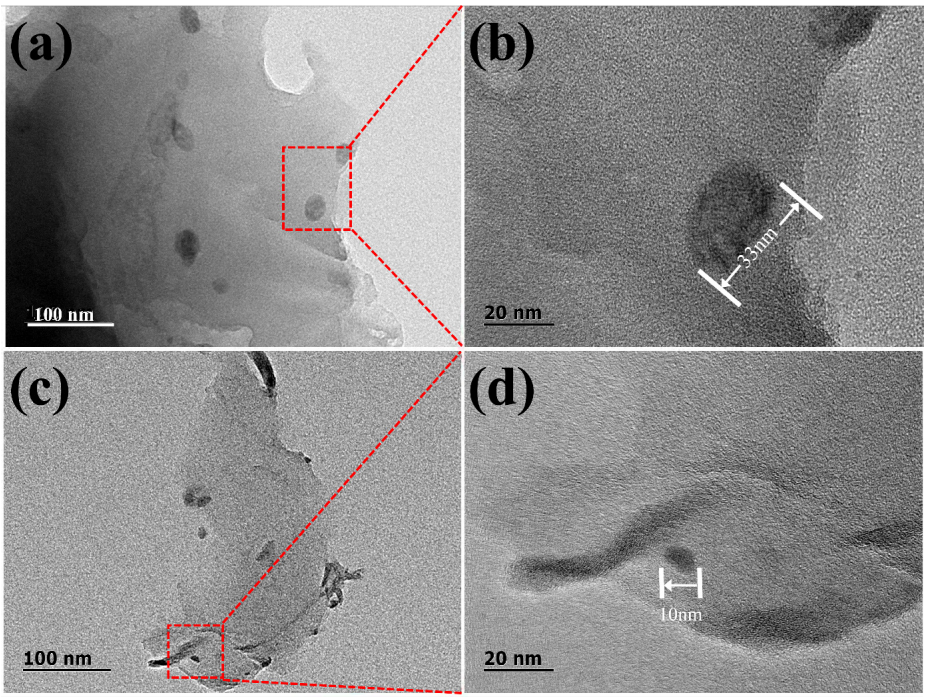

Figure 3. TEM image of GO/Cu-MOF-300 (a) and its local enlargement (b) and of GO/Cu-MOF-400 (c) and its local enlargement (d)

GO/Cu-MOF-300 and GO/Cu-MOF-400 were also characterized by Transmission electron microscope (TEM) after natural cooling. GO/Cu-MOF-400 had a particle size of about 10 nm (Figure 3(d)), less than for 300 ℃ (33 nm) (Figure 3(b)). The two-dimensional layered structure of GO can also be clearly seen from the images, with a smooth surface and copper nanoclusters attached to the GO surface.

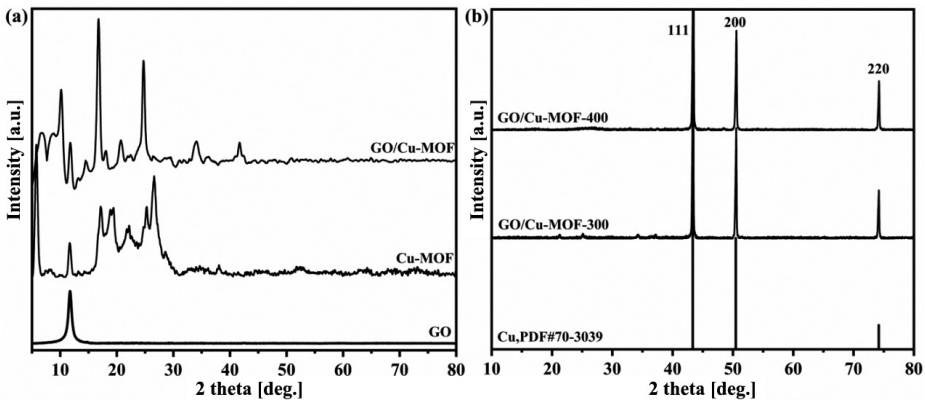

Figure 4. XRD patterns of GO, Cu-MOF and GO/Cu-MOF composites (a) and after calcination GO/Cu-MOF-300 and GO/Cu-MOF-400 (b)

Typical XRD patterns of GO, Cu-MOF and GO/Cu-MOF composites are shown in Figure 4(a). It can be seen that GO exhibits only one peak at $2\theta = 11.7°$, and the diffraction peak intensity is high, indicating that GO has a high purity. When the Cu-MOF material is combined with GO, part of the GO is reduced to RGO (Raw GO), which results in the characteristic diffraction peak of GO at $2\theta = 24.7°$ at high temperature. It was found that in the GO/Cu-MOF composite, the peak position of GO (10.2°) to the left. According to Bragg›s formula, the increase of the graphene oxide layer spacing after ultrasonic treatment is conducive to catalyst insertion [26]. In addition, the peak positions of GO/Cu-MOF is similar to that of Cu-MOF, and the noise wave is less, indicating that GO/Cu-MOF composite have been successfully synthesized.

The XRD patterns of the GO/Cu-MOF-300 and GO/Cu-MOF-400 samples after calcination are shown in Figure 4(b). Obviously, the diffraction peaks appear in different positions from GO/Cu-MOF, and the characteristic diffraction peaks of $2\theta = 43.35°$, 50.57° and 74.22° can correspond to three crystal faces of CuPDF#70-3039 (111), (200) and (220) [27]. This result shows that part of the Cu(II) has been reduced to Cu(0) under high temperature calcination and further forms Cu nanoclusters.

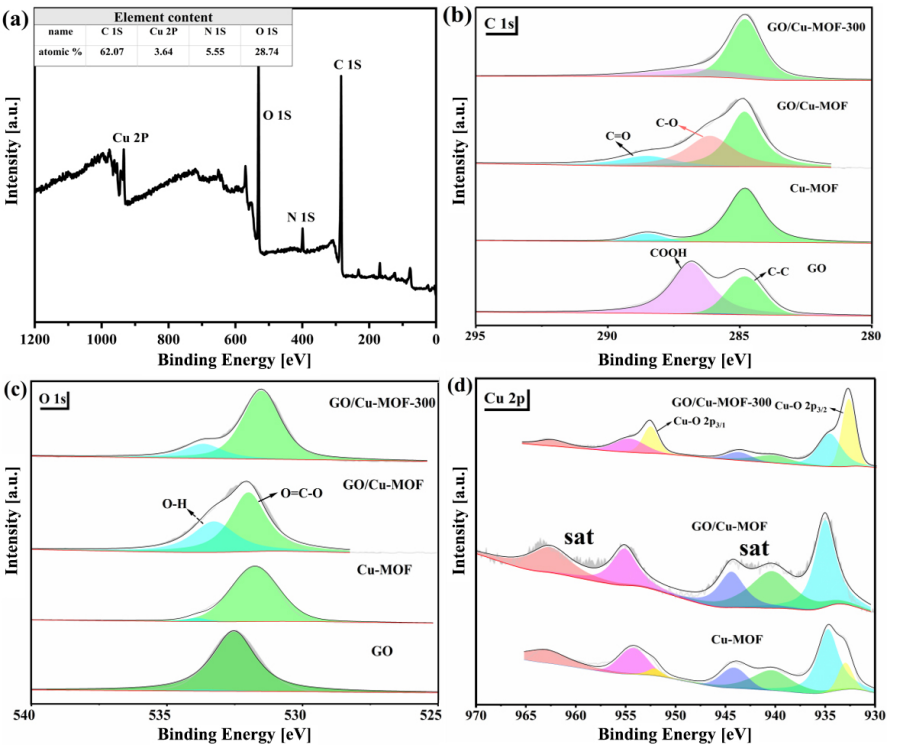

Figure 5. XPS spectrum of GO/Cu-MOF composites (a) and high-resolution XPS spectra of C1s, O1s, and Cu2p of GO, Cu-MOF, GO/Cu-MOF and GO/MOF-300 (b-d, respectively)

The surface chemical composition and electronic states of GO, Cu-MOF, GO/Cu-MOF and GO/Cu-MOF-300 were further studied by XPS. As shown in Figure 5(a), four elements C, O, N and Cu coexist in GO/Cu-MOF composites, and the content of Cu is 3.64%. Figures 5(b-d) show the high-resolution XPS spectra of C1s, O1s, and Cu2p for GO, GO/Cu-MOF, and GO/CU-MOF-300, respectively. It can be seen from the C spectrum (Figure 5(b)) that the positions of the binding energies of 284.8 and 286.8 eV correspond to the main ring structure of graphene oxide and the carboxyl groups in the oxygen-containing functional groups, respectively. With the addition of Cu-MOF, a carbon group (C–O) appeared in the ligand, with a binding energy of 286.1 eV.

The high-resolution O1s spectrum in Figure 5(c) can be divided into two component peaks, except for GO, corresponding to the carboxyl group (O=C–O) and hydroxyl group (O–H) in the ligand in the GO/Cu-MOF composite, with binding energies of 531.9 and 533.2 eV, respectively. After heat treatment at

300 °C, the XPS peak of the carboxyl group shifts to the right, the peak of the hydroxyl group shifts to the left, and the binding energy of the O element increases, which may be due to the coordination between these two groups and copper ions.

Figure 5(d) provides a detailed analysis of the Cu2p high-resolution spectra of Cu-MOF, GO/Cu-MOF, and GO/CU-MOF-300. The main peaks of $Cu2p_{1/2}$ at 955.1 and 935.0 eV shows the oxidation state of Cu^{2+}, while three concomitant peaks of Cu^{2+} appear near the binding energies of 962.6, 944.4 and 940.4 eV respectively. This may be due to the oxidation of the sample by air to form a new CuO substance. Yan *et al.* [28] also found that Cu-MOF formed a small amount of CuO under high temperature calcination. In addition, the binding energy of Cu(II) in GO/Cu-MOF-300 samples is exactly the same as that of pure Cu-MOF, which further confirms that Cu(II) also contains the coordination of Cu^{2+} with carboxyl groups.

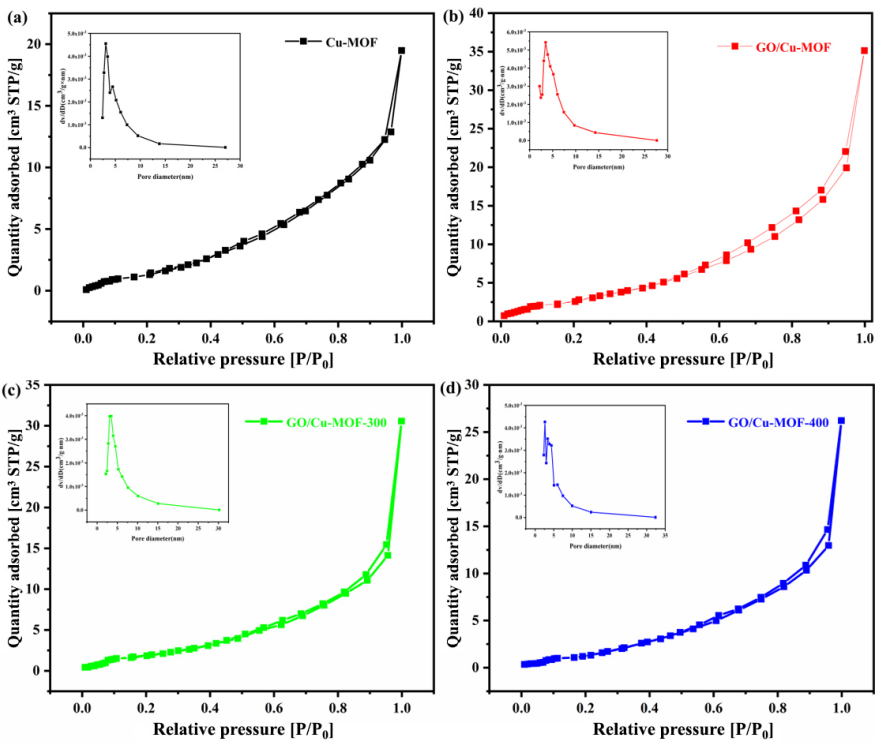

Figure 6. N_2 adsorption-desorption isotherm of Cu-MOF (Inset: pore diameter distribution of Cu-MOF) (a), and GO/Cu-MOF (Inset: pore diameter distribution of GO/Cu-MOF) (b), GO/Cu-MOF-300 (Inset: pore diameter distribution of GO/Cu-MOF-300) (c) and GO/Cu-MOF-400 (Inset: pore diameter distribution of GO/Cu-MOF-400) (d)

The specific surface area and pore size distribution of Cu-MOF, GO/Cu-MOF and the calcined samples were characterized by their N_2 adsorption-desorption isotherms, and their catalytic effects on RDX decomposition were further studied. It can be seen from Figure 6 that all N_2 adsorption-desorption curves have hysteresis loops and follow a type III adsorption, which is characterized by mesoporous presence. The illustrated aperture distribution curve shows that the average particle size of all samples was between 2.5-3.5 nm. The adsorption capacity in the low pressure region was small, and the adsorption capacity increased rapidly after P/Po = 0.8. The results showed that the greater the relative pressure, the greater the adsorption capacity. After adding GO, the specific surface area of the composite GO/Cu-MOF increased from the original 6.177 to 11.829 m^2/g, as shown in Figure 6(b). This is because GO obstructs the agglomeration of the Cu-MOF, increases the specific surface area and the active sites of the reactants, and further affects the catalytic effect on RDX. In addition, the specific surface area and pore volume decreased with an increase in calcination temperature. This is due to the collapse of part of the porous structure in the GO/Cu-MOF, the pores are destroyed, and the presence of GO covers the surface and interior of the channels. As can be seen from Figure 6(c), the specific surface area of GO/Cu-MOF-300 reaches 8.452 m^2/g, and the average particle size is 3.1 nm. This observation also confirms that GO/Cu-MOF-300 is composed of mesopores. All of these indicate that GO/Cu-MOF-300 has a large specific surface area and an abundant pore structure, which can increase the contact area with RDX and provide more active sites for the thermal decomposition of RDX. Specific relevant parameters are listed in Table 1.

Table 1. N_2 adsorption-desorption parameters of Cu-MOF, GO/Cu-MOF, GO/Cu-MOF-300 and GO/Cu-MOF-400

Sample	BET surface area [m^2/g]	Pore volume [cm^3/g]	Average pore diameter [nm]
Cu-MOF	6.177	0.035	3.1258
GO/Cu-MOF	11.829	0.062	3.4639
GO/Cu-MOF-300	8.452	0.051	3.1072
GO/Cu-MOF-400	6.814	0.046	2.6372

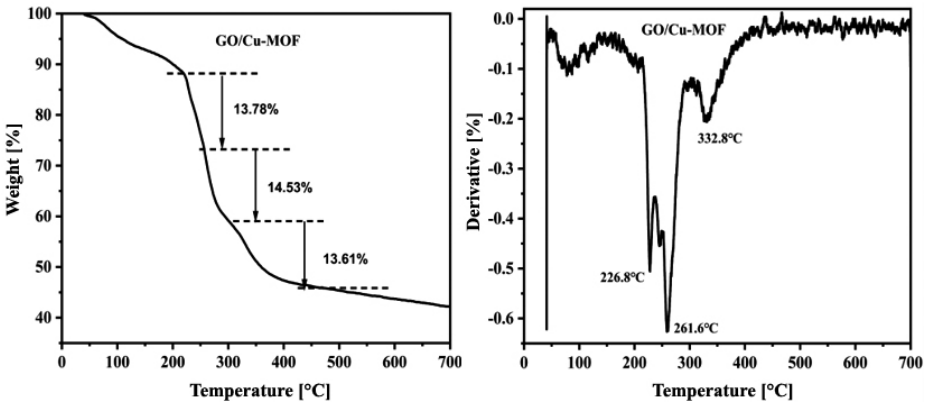

(a) (b)

Figure 7. TGA (a) and DTG (b) curves of GO/Cu-MOF composites

In order to determine the best calcination temperature for the sample, the decomposition process of GO/Cu-MOF composites under N_2 atmosphere and flow rate of 5 mL·min^{-1} from ambient to 700 °C under normal pressure was studied by TGA thermogravimetric analysis, as shown in Figure 7. The TGA thermogram of GO/Cu-MOF (Figure 7(b)) exhibited three stages of weight loss at temperatures of 226.8, 261.6 and 332.8 °C. Of these, 226.8 °C corresponds to the temperature for the loss of bound water in $CuSO_4 \cdot 5H_2O$. With the increase in temperature, the organic ligand began to collapse at 261.6 °C, became partially degraded, and completely decomposed at 332.8 °C, which was consistent with the analysis results in Figure 2. Therefore, 300 and 400 °C were judged to be the best calcination temperatures for the samples.

3.2 The effect of Cu-MOF, GO/Cu-MOF, GO/Cu-MoF-300, and GO/Cu-MOF-400 on the thermal decomposition performance of RDX

The raw material RDX was studied by DSC. RDX/GO/Cu-MOF, RDX/GO/Cu-MoF-300, RDX/GO/Cu-MOF-400 nanocomposites were studied from room temperature to 300 °C at a N_2 flow rate of 20 mL/min, and at different heating rates (5, 10, 15 and 20 K/min). From all four curves (Figure 8), it can be seen that there is an endothermic peak at about 206 °C, which is caused by the crystalline transformation of RDX. At the same heating rate (Figure 8(a)), the catalytic effect on RDX of the catalyst GO/Cu-MOF-300, formed by calcination at 300 °C, is better than that of GO/Cu-MOF-400, calcined at 400 °C. This may be due to the formation of copper atomic clusters and the presence of

uncollapsed ligands at 300 °C, which accelerate the electron transfer, increase the active sites for RDX, advance the exothermic peak of RDX, make the exothermicity of RDX more concentrated, and improve the degree of thermal decomposition of RDX. Some of the specific data involved are listed in Table 2. It can be seen from the table that for the same substance, the heat release temperature of RDX gradually increases with the increase in heating rate. The increase in the heating rate will increase the temperature difference between the surface and the interior of the RDX particles, enhance the inertial effect of devolatilization, and lead to the degradation of the particles and an increase of the peak temperature of the DSC curve [29].

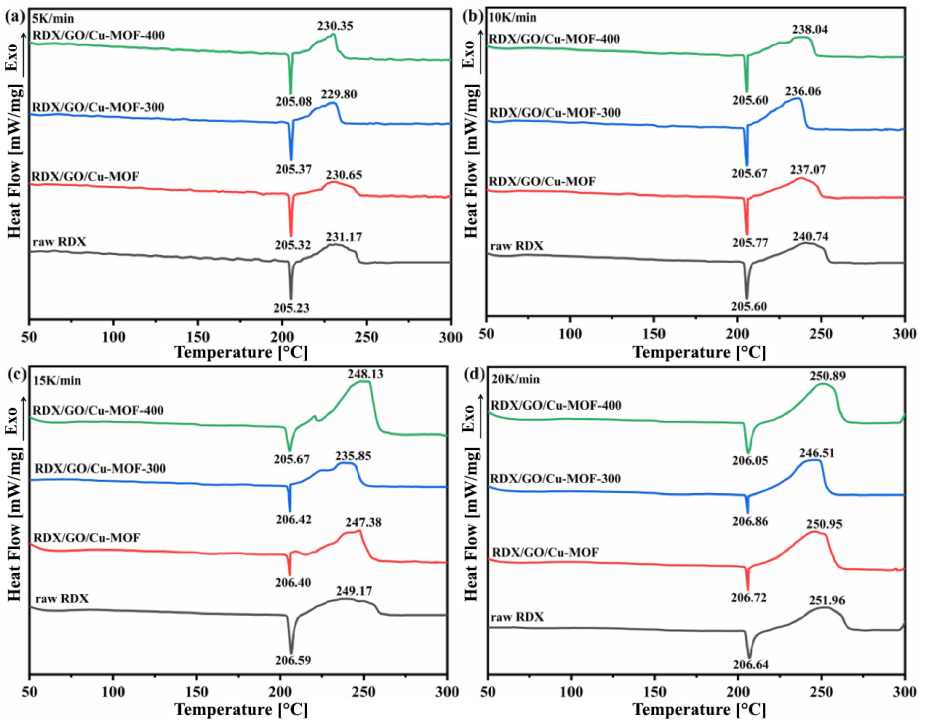

Figure 8. DSC curves of the different samples (raw RDX, RDX/GO/Cu-MOF, RDX/GO/Cu-MOF-300, RDX/GO/Cu-MOF-400) at the same heating rates 5 (a), 10 (b), 15 (c) and 20 K/min (d)

Table 2. The results of the catalytic activity of various samples

Sample	Heating rate [°C min^{-1}]	T_{en} [°C]	T_{ex} [°C]
raw RDX	5	205.23	231.17
	10	205.60	240.74
	15	206.59	249.17
	20	206.64	251.96
RDX/GO/Cu-MOF	5	205.32	230.65
	10	205.77	240.74
	15	206.40	247.38
	20	206.72	250.95
RDX/GO/Cu-MOF-300	5	205.37	229.80
	10	205.67	236.06
	15	206.42	235.85
	20	206.86	246.51
RDX/GO/Cu-MOF-400	5	205.08	230.85
	10	205.60	238.04
	15	205.67	248.13
	20	206.05	250.89

Note : T_{en} and T_{ex} stand for endothermic and exothermic peaks, respectively

In order to further study the catalytic effect of the prepared catalysts on RDX, the apparent activation energy of the RDX/catalyst samples at different conversion was calculated by the Kissinger method [30], as shown in Figure 9. It is clear that all catalysts have an obvious catalytic effect on RDX. Of these, the apparent activation energy of GO/Cu-MOF-300 for RDX decomposition is decreased significantly, and this catalytic effect was the best achieved. The effect of GO/Cu-MOF-300 on RDX decomposition is maximal compared with the original RDX and the other RDX/catalyst samples, which further indicates that the catalytic effect of the 300 °C calcined sample is the best.

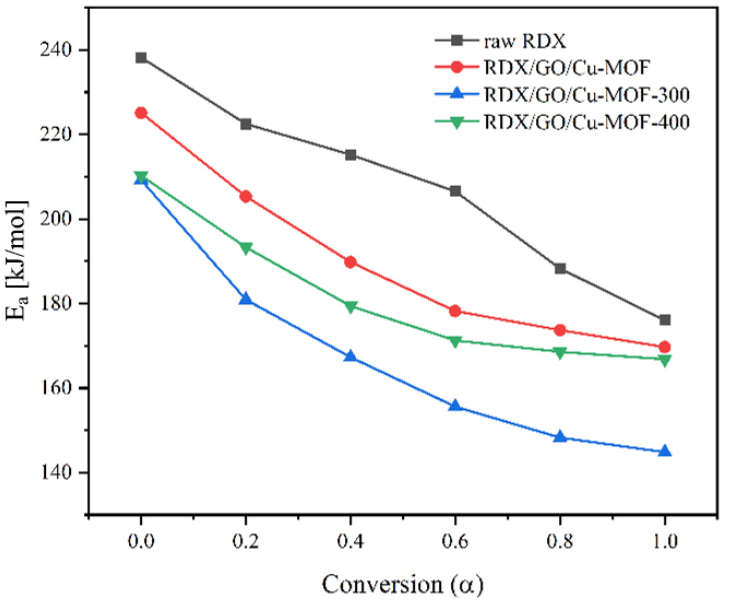

Figure 9. The apparent activation energies (E_α) *vs* conversion (α)

3.3 Analysis of the RDX thermal decomposition mechanism

There have been many studies on the thermal decomposition mechanism of RDX [31, 32]. The step-by-step thermal decomposition equation for RDX is shown in Figure 10. During the thermal decomposition process, when RDX is heated the N–N, N–C bonds break first. After electron transfer, the molecular fragments of RDX react further under electron bombardment. When Cu-MOF and GO are present, the thermal decomposition rate of RDX is increased because they accelerate the transfer of electrons during the thermal decomposition, thus promoting the thermal decomposition. As a catalytically active substance, Cu ions in GO/Cu-MOF-300 can also easily absorb electrons in empty orbitals and further release them at higher temperatures, thus accelerating electron transfer. In addition, the large specific surface area of GO not only effectively inhibits the agglomeration of Cu-MOF, but also significantly increases the catalytic active sites of Cu-MOF. The "positive synergistic effect" formed by the combination of GO/Cu-MOF-300 composites greatly improves the catalytic thermal decomposition performance of RDX.

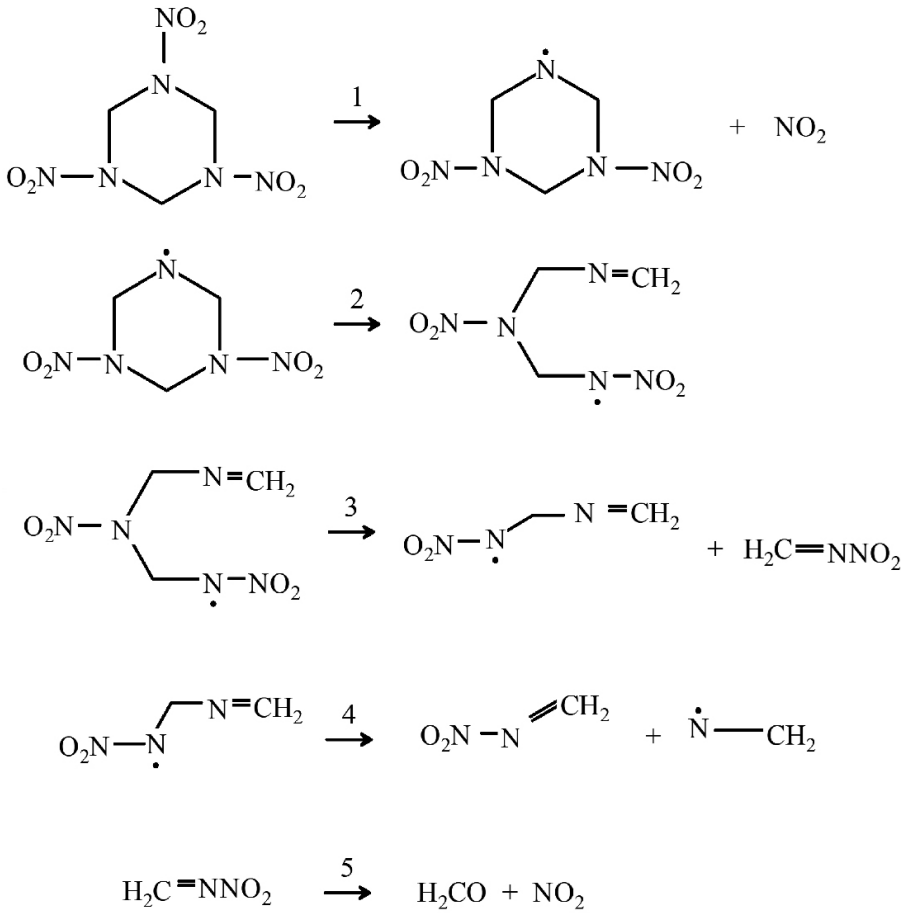

Figure 10. The step-by-step decomposition of RDX

4 Conclusions

- The graphene based Cu-MOF derivative catalyst was successfully prepared by the method of solution heat and heat treatment. The crystal structure of the Cu-MOF composite was not changed by the addition of GO, and Cu-MOF was uniformly dispersed on the GO nanosheets. Due to its large specific surface area, the agglomeration problem of Cu-MOF is effectively suppressed, and the specific surface area of the composite is also increased, which in turn increases the catalytic activity of the composite on the thermal decomposition of RDX.

- Furthermore, the DSC results demonstrated that the addition of a small amount of GO/Cu-MOF-300 reduced the decomposition temperature of RDX by 4.67 °C (10 °C/min), and accelerated the decomposition rate of RDX to a certain extent. Cu nanoclusters bind to the surface of RDX *via* the Cu–O bond, which increases the active sites for RDX thermal decomposition. At the same time, the excellent electrical conductivity of GO accelerates the speed of electron transfer, increases the active sites for RDX thermal decomposition, and shows excellent performance in catalytic RDX thermal decomposition.

Acknowledgements

This work was financially supported by the Natural Science Foundation of Shanxi Province (No. 202203021221120).

References

[1] Naya, T.; Kohga, M. Influences of Particle Size and Content of RDX on Burning Characteristics of RDX-based Propellant. *Aerosp. Sci. Technol.* **2014**, *32*(1): 26-34; https://doi.org/10.1016/j.ast.2013.12.004.

[2] Liang, T.X.; Zhang, Y.K.; Ma, Z.L.; Guo, M.L.; Xiao, Z.L.; Zhang, J.X.; Dong, M. Y.; Fan, J.C.; Guo, Z.H.; Liu, C.T. Energy Characteristics and Mechanical Properties of Cyclotrimethylenetrinitramine (RDX)-based Insensitive High-Energy Propellant. *J. Mater. Res. Technol.* **2020**, *9*(6): 15313-15323; https://doi.org/10.1016/j.jmrt.2020.09.132.

[3] Babuk, V.A.; Ivonenko, A.N.; Nnizyaev, A.A. Calculation of the Characteristics of Agglomerates During Combustion of High-Energy Composite Solid Propellants. *Combust. Explos. Shock Waves* **2015**, *51*(5): 549-559; https://doi.org/10.1134/s0010508215050056.

[4] Zhao, G.; Lu, M. Theoretical Studies on the Structures and Detonation Properties of Nitramine Explosives Containing Benzene Ring. *J. Mol. Model.* **2012**, *18*(6): 2443-2451; https://doi.org/10.1007/s00894-011-1267-1.

[5] Han, S.; Kim, C. Integrated Fluid-Structure Simulation for Full Burning of a Solid-Propellant Rocket Interior. *J. Propul. Power* **2014**, *30*(4): 883-900; https://doi.org/10.2514/1.B35107.

[6] Liu, R.; Zhang, T.; Yang, L.; Zhou, Z. Dynamic Pressure Thermal Analysis of Double-base Propellants Containing RDX. *Cent. Eur. J. Chem.* **2014**, *12*(6): 672-677; https://doi.org/10.2478/s11532-014-0524-4.

[7] Li, G.P.; Ni, Z.C.; Liu, Y.Z.; Xia, M.; Luo, Y.J. Thermal Performance and Decomposition Kinetics of RDX/AP/SiO_2 Intermolecular Explosive. *J. Therm. Anal. Calorim.* **2018**, *132*(3): 1969-1978; https://doi.org/10.1007/s10973-018-7049-6.

[8] Feng, S.Q.; Guo, F.; Yuan, C.S.; Cheng, X.R.; Wang, Y.Q.; Zhang, H.J.; Chen, J; Su, L. Effect of Neutron Irradiation on Structure and Decomposition of α-RDX: A ReaxFF Molecular Dynamics Study. *Comput. Theor. Chem*. **2023**, *1219* paper 113965; https://doi.org/10.1016/j.comptc.2022.113965.

[9] Chaturvedi, S.; Dave, P.N. A Review on the Use of Nanometals as Catalysts for the Thermal Decomposition of Ammonium Perchlorate. *J. Saudi Chem. Soc.* **2013**, *17*(2): 135-149; https://doi.org/10.1016/j.jscs.2011.05.009.

[10] Zhu, Y.L.; Huang, H.; Ren, H.; Jiao, Q.J. Influence of Aluminum Particle Size on Thermal Decomposition of RDX. *J. Energ, Mater.* **2013**, *31*(3): 178-191; https://doi.org/10.1080/07370652.2012.688788.

[11] Xiong, F.; Xu, R.; Nie, H.; Yan, Q.; Wu, Y.; Liu, J.; Chen, J.; Sun, Y. Mechanistic Study of the Influence of Aluminum Nanoparticles on the Pressure Sensitivity of 1,3,5-Trinitro-1,3,5-triazinane (RDX) Thermal Decomposition. *Colloids Surf., A* **2023**, *667* paper 132439; https://doi.org/10.1016/j.colsurfa.2023.132439.

[12] Yan, Q.L.; Zhao, F.Q.; Kuo, K.K.; Zhang, X.H.; Zeman, S.; DeLuca, L.T. Catalytic Effects of Nano Additives on Decomposition and Combustion of RDX-, HMX-, and AP-based Energetic Compositions. *Prog. Energy Combust. Sci.* **2016**, *57*: 75-136; https://doi.org/10.1016/j.pecs.2016.08.002.

[13] Song, N.; Liu, J.; Yang, L.; Liu, P. Preparation of Nano-Spherical Cu-en and Its Catalytic Study on the Performance of Solid Propellant. *Propellants Explos., Pyrotech.* **2020**, *45*(11): 1799-1804; https://doi.org/10.1002/prep.202000147.

[14] Kou, Y.; Luo, P.; Xiao, L.; Xin, Y.; Zhang, G.; Hu, Y.; Yang, J.; Gao, H.; Zhao, F.; Jiang, W.; Hao, G. New Insights in Nano-Copper Chromite Catalyzing Ultrafine AP: Evaluation of Dispersity and Mixing Uniformity. *Def. Technol.* **2024**, *32*: 120-133; https://doi.org/10.1016/j.dt.2023.04.004.

[15] Nie, H.; Yang, X.H.; Yang, S.L.; Fershtat, L.; Yan, Q.L. The Enhanced Catalytic Decomposition Behaviors of RDX by Using Porous Activated Carbon Loaded with Nanosized Metal Oxides. *J. Therm. Anal. Calorim.* **2023**, *148*(10): 4255-4266; https://doi.org/10.1007/s10973-023-11987-8.

[16] Liu, B.; Wang, W.; Wang, J.; Zhang, Y.; Xu, K.; Zhao, F. Preparation and Catalytic Activities of $CuFe_2O_4$ Nanoparticles Assembled with Graphene Oxide for RDX Thermal Decomposition. *J. Nanopart. Res.* **2019**, *21* paper 48; https://doi.org/10.1007/s11051-019-4493-6.

[17] Dong, S.; Hu, J.; Qin, Z.; Li, H.; Chen, S.; Chen, Z.; Xu, K. Design and Performance of a Novel High-Efficiency WO_3-based Combustion Catalyst and Its Catalytic Mechanism. *Appl. Surf. Sci.* **2023**, *624* paper 157130; https://doi.org/10.1016/j.apsusc.2023.157130.

[18] Chen, C.; Lu, J.; Zhang, B.; Gou, X.; Wu, T.; Chen, Z.; Liu, W.; Zhang, J.; Liang, T.; Yang, Y.; Xiao, F. Study on the Effect of Graphite-based Materials on the Reactivity of Activated Aluminum Composites in Different Forms of Water. *J. Cleaner Prod.* **2024**, *435* paper 140607; https://doi.org/10.1016/j.jclepro.2024.140607.

[19] Hong, C.; Jin, X.; Totleben, J.; Lohrman, J.; Harak, E.; Subramaniam, B.; Chaudhari, R.; Ren, S. Graphene Oxide Stabilized Cu_2O for Shape Selective Nanocatalysis.

J. Mater. Chem. A **2014**, *2*(20): 7147-7151; https://doi.org/10.1039/c4ta00599f.
[20] Wan, C.; Li, J.; Chen, S.; Wang, W.; Xu, K. *In situ* Synthesis and Catalytic Decomposition Mechanism of $CuFe_2O_4$/g-C_3N_4 Nanocomposite on AP and RDX. *J. Anal. Appl. Pyrolysis* **2021**, *160* paper 105372; https://doi.org/10.1016/j.jaap.2021.105372.
[21] Wang, W.; Liu, B.; Xu, K.; Zu, Y.; Song, J.; Zhao, F. *In-situ* Preparation of $MgFe_2O_4$-GO Nanocomposite and Its Enhanced Catalytic Reactivity on Decomposition of AP and RDX. *Ceram. Int.* **2018**, *44*(15): 19016-19020; https://doi.org/10.1016/j.ceramint.2018.07.145.
[22] Kottappara, R.; Pillai, S.C.; Vijayan, B.K. Copper-based Nanocatalysts for Nitroarene Reduction – A Review of Recent Advances. *Inorg. Chem. Commun.* **2020**, *121* paper 108181; https://doi.org/10.1016/j.inoche.2020.108181.
[23] Mantasha, I.; Saleh, H.A.M.; Qasem, K.M.A.; Shahid, M.; Mehtab, M.; Ahmad, M. Efficient and Selective Adsorption and Separation of Methylene Blue (MB) from Mixture of Dyes in Aqueous Environment Employing a Cu(II) Based Metal Organic Framework. *Inorg. Chim. Acta* **2020**, *511* paper 119787; https://doi.org/10.1016/j.ica.2020.119787.
[24] Chen, Y.; Huang, N.; Liang, Y. Preparation of CeO_2/Cu-MOF/GO Composite for Efficient Electrocatalytic Oxygen Evolution Reaction. *Ionics* **2021**, *27*(10): 4347-4360; https://doi.org/10.1007/s11581-021-04173-z.
[25] Deng, N.; Wang, L.; Feng, Y.; Liu, M.; Li, Q.; Wang, G.; Zhang, L.; Kang, W.; Cheng, B.; Liu, Y. Co-based and Cu-based MOFs Modified Separators to Strengthen the Kinetics of Redox Reaction and Inhibit Lithium-Dendrite for Long-Life Lithium-Sulfur Batteries. *Chem. Eng. J.* **2020**, *388* paper 124241; https://doi.org/10.1016/j.cej.2020.124241.
[26] Kitamura, H. Semi-Analytic Theory of Multiphonon Effects on the Static Structure Factors of Warm Solids. *Acta Crystallogr., Sect. A* **2022**, *78*: 415-421; https://doi.org/10.1107/s2053273322006441.
[27] Juskenas, R.; Avizinis, D.; Kalinauskas, P.; Selskis, A.; Giraitis, R.; Pakstas, V.; Karpaviciene, V.; Kanapeckaite, S.; Mockus, Z.; Kondrotas, R. XRD, SEM and photoelectrochemical characterization of ZnSe electrodeposited on Cu and Cu-Sn substrates. *Electrochim. Acta* **2012**, *70*: 118-123; https://doi.org/10.1016/j.electacta.2012.03.103.
[28] Yan, J.; Wang, H.; Jin, B.; Zeng, M.; Peng, R. Cu-MOF Derived Cu/Cu_2O/C Nanocomposites for the Efficient Thermal Decomposition of Ammonium Perchlorate. *J. Solid State Chem.* **2021**, *297* paper 122060; https://doi.org/10.1016/j.jssc.2021.122060.
[29] Bai, F.; Guo, W.; Lu, X.; Liu, Y.; Guo, M.; Li, Q.; Sun, Y. Kinetic Study on the Pyrolysis Behavior of Huadian Oil Shale via Non-Isothermal Thermogravimetric Data. *Fuel* **2015**, *146*: 111-118; https://doi.org/10.1016/j.fuel.2014.12.073.
[30] Blaine, R.L.; Kissinger, H.E. Homer Kissinger and the Kissinger Equation. *Thermochim. Acta* **2012**, *540*: 1-6; https://doi.org/10.1016/j.tca.2012.04.008.
[31] Yuan, S.; Li, Z.Q.; Luo, Q.P.; Duan, X.H.; Pei, C.H. Preparation and Thermal

Decomposition Properties of Nitrated Graphene Oxide (NGO)/RDX nano-Energetic Composites. *J. Therm. Anal. Calorim.* **2020**, *139*(3): 1671-1679; https://doi.org/10.1007/s10973-019-08613-x.

[32] Fang, Z.Q.; Li, S.K.; Liu, J.P.; Yu, C.; Zheng, D.S.; Qiao, M.Z. Effect and Mechanism of Lithium Aluminium Hydride on the Pyrolysis Process of RDX. *J. Anal. Appl. Pyrolysis* **2022**, *167* paper 105690; https://doi.org/10.1016/j.jaap.2022.105690.

Contribution

Zhang J.: foundations, performing the experimental part
Liang T.: conception, methods, performing statistical analysis

Received: October 17, 2024
Revised: December 17, 2024
First published online: December 20, 2024